Pressure-driven symmetry transitions in dense H_2O ice

Zachary M. Grande,[1] C. Huy Pham,[2] Dean Smith,[1,3] John H. Boisvert,[1] Chenliang Huang,[1,4] Jesse S. Smith,[3] Nir Goldman,[2] Jonathan L. Belof,[2] Oliver Tschauner,[5] Jason H. Steffen,[1] and Ashkan Salamat[1,*]

[1]*Department of Physics and Astronomy, University of Nevada Las Vegas, Las Vegas, Nevada 89154, USA*
[2]*Lawrence Livermore National Laboratory, 7000 East Ave., Livermore, California 94550, USA*
[3]*HPCAT, X-ray Science Division, Argonne National Laboratory, Argonne, Illinois 60439, USA*
[4]*Lunar and Planetary Laboratory, University of Arizona, Tucson, Arizona 85721, USA*
[5]*Department of Geoscience, University of Nevada Las Vegas, Las Vegas, Nevada 89154, USA*

(Received 9 December 2021; revised 18 February 2022; accepted 24 February 2022; published 17 March 2022)

X-ray diffraction and Raman spectroscopy of H_2O (ice) structures are measured under static compression in combination with grain normalizing heat treatment via direct laser heating. We report the transition from cubic ice-VII to a structure of tetragonal symmetry, ice-VII_t at 5.1 ± 0.5 GPa. This is succeeded by the H-bond symmetrization transition occurring at a pressure of 30.9 ± 3 GPa. Both experimental observations are supported by simulated Raman spectra from density-functional theory quantum calculations. The transition to H-bond symmetrization is evidenced by the reversible emergence of its characteristic Raman mode and a 2.5-fold increase in bulk modulus, implying a significant increase in bonding strength.

DOI: 10.1103/PhysRevB.105.104109

I. INTRODUCTION

The pressure-temperature phase diagram of H_2O exhibits a remarkable number of polymorphic transitions [1,2]. At low pressures, this complexity arises from steric rearrangements of hydrogen-bonded (H-bond) molecules, while the H–O–H bond angle and length remain almost constant. H bonds are established through correlated disorder of the protons between adjacent oxygen atoms such that, at each moment, two protons and one oxygen form an H_2O molecule [3]. Condensed H_2O (ice) structures generally exhibit networklike topologies similar to those of silica and silicates [4]. The behavior of these ice phases is dominated by this H-bond network.

Above 2.1 GPa and 300 K, ice-VII is the stable crystalline phase of H_2O. However, rather than transforming into further dense packed networks of H-bonded structures with increasing pressure, the H bond becomes gradually weaker [5]. In this case, the protons migrate to a symmetric position [6,7], resulting in a transition to a mixed covalent/ionic O–H bond in ice-X. This mechanism is observable through infrared spectroscopy as a gradual softening of the antisymmetric O–H stretching vibration and its eventual disappearance observed above 60 GPa [8,9], combined with a stiffening of lower frequency lattice and librational modes [10]. The bond strength in the mixed covalent/ionically bonded ice-X should differ from the H-bonded regime of ice-VII, resulting in a significantly lower compressibility. While this fundamental change in O–H bond character is generally accepted, there remain large uncertainties on the phase boundary between ice-VII and ice-X, with reported transition pressures ranging from 40 GPa to above 120 GPa [8,9,11–19]. This can have large ramifications for equation of state (EOS) models and studies of planetary interiors, where precise knowledge of these physical properties are needed for accurate interpretation of astronomical observations [20,21].

The substantial range in claims for the transition pressure to ice-X is largely due to the gradual nature of the transition which may have as many as two intermediate structures to facilitate the H-bond symmetrization [11,14,16,18,22]. Proton nuclear magnetic resonance (or H NMR) experiments directly probe the local environment of the H bond of water, providing a more detailed model of the energy potential [18]. The potential, which is widely agreed upon, starts from a double well in ice-VII and as the density is increased it is gradually deformed and the barrier becomes increasingly shallow allowing for the proton tunneling rate to increase. This delocalizes the proton and gives it an average position between the two wells. Calculations by Trybel *et al.* [23] have further explored such delocalization effects of the proton and how effective ionization of the water molecule can play a significant role in shaping the energy potential of the H bond. Additionally, analysis of the bulk modulus during quasidynamic compression up to 180 GPa has been interpreted as showing transitions for ice-VII to disordered ice-VII′ and then to a disordered ice-X′ before the fully symmetrized ice-X [22].

Structural measurements (x-ray and neutron diffraction) have shown anomalies in the 10–14 GPa regime typically relating to proton/deuteron dynamics [11,14,16,24,25], which have been coined as the proton-disordered ice-VII′ phase. However, until now these claims have lacked support from spectroscopic evidence. These claims are largely based on measurements that show deviations or features not accommodated by the presumed cubic structure for ice-VII; at least one such anomaly has been suggested to result from a tetragonal distortion [14]. Neutron diffraction studies on D_2O have shown that the deuterons occupy sites inconsistent with the present ice-VII model [16] and, in the transition to ice-VIII

*salamat@physics.unlv.edu

at lower temperatures, the oxygen sites become disordered as well as the deuteron sites [26].

Exploring the structure of different isotopes of water ice becomes even more complex because bond states in soft molecular compounds are strongly affected by the anisotropic strain that results from applying nonhydrostatic stress. Thus, the phase boundary into ice-X may shift, depending upon the nature of the nonhydrostatic stresses for a given experiment and on the length scale of a given diagnostic probe. H_2O/D_2O measurements are especially susceptible to such conditions since using a pressure transmitting medium to establish hydrostatic equilibrium would contaminate the sample by formation of hydrates and clathrates. The resulting distortions are further exacerbated by the heterogeneous nucleation of ice-VII in ice-VI, which tends to produce large domains with a preferred orientation and create anisotropic strain and shearing at grain boundaries. This gives rise to significant texturing and broadening of Bragg peaks in x-ray diffraction (XRD) [27].

II. METHODS

Our observations support the occurrence of two pressure-driven symmetry transitions after ice-VII at room temperature below a megabar. These claims are supported by a combination of pressure-volume EOS measurements, Raman spectroscopy and density functional theory (DFT) calculations. Experimental compression data is acquired by using a diamond anvil cell (DAC) of custom design, driven by a gas membrane. Liquid H_2O (electrophoresis and spectroscopic grade; Sigma-Aldrich) is loaded into sample chambers formed by laser micromachining [28] accompanied by a $\sim 10\,\mu$m piece of polycrystalline Au to serve as a pressure marker. To avoid reactions between the heated H_2O and the Re gasket, we line the inside of our sample chamber with Pt [29]. We perform powder XRD at the HPCAT diffraction beamline (Sector 16-ID-B, Advanced Photon Source, Argonne National Laboratory, IL, USA) ($\lambda = 0.40663$ Å). Raman spectroscopy experiments are performed at University of Nevada Las Vegas (UNLV) using the same sample preparation technique and a Ar-Kr laser lasing at 514.5 nm to excite the sample. We report spectroscopic data on the lattice modes of ice from 100 to 1000 cm^{-1} but not the molecular stretching modes above 2000 cm^{-1} due to overlap with the second-order diamond signal at higher pressures.

To improve sample quality, we utilize the high absorbance of ice in the midinfrared to melt the ice sample and then let it cool back to ambient temperature. $10.6\,\mu$m radiation from a Synrad *Evolution*125 CO_2 laser is focused to a minimum spot size $\sim 30\,\mu$m and directly absorbed by the compressed sample, using an instrument built in place at the diffraction beamline [30] or on a system housed at UNLV. Visible imaging confirms the melting and dynamic recrystallization of powdered ice [29]. The cooling rate after melting is such that it promotes a normalized grain size and random orientation which is analogous to metallurgical normalization techniques [31]. The focused beam is translated throughout the sample chamber to make a homogeneous sample and relieve anisotropic strain from both the powdered ice and the Au pressure marker. The reduced domain sizes of the ice and their random orientations yield well-resolved Debye-Scherrer rings

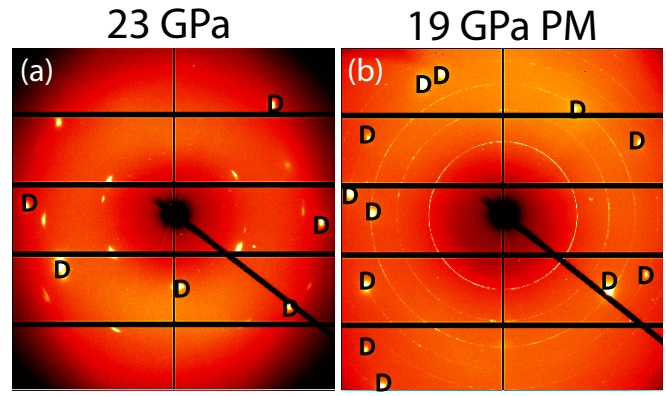

FIG. 1. 2-D x-ray diffraction images. (a) 2D diffraction image of ice at 23 GPa with no heat treatment displaying high degree of texturing and broadening of multigrain peaks. (b) 2D diffraction image of ice at 19 GPa post melt (PM) showing full Debye-Scherrer rings for an extensive q range with minimal broadening.

for an extensive q range [Fig. 1(b)], making our data suitable for Rietveld powder XRD analysis. Data from samples that are not heat treated display significantly fewer diffraction features and typically exhibit multigrain spots or highly textured rings with significant peak broadening from deviatoric strain. This is shown in Figs. 1(a) and 1(b), where the FWHM of the (1 1 0) peak improves from 0.24 to 0.088° 2θ in the heat treated pattern. The powdered nature of the sample also reduces its susceptibility to further deviatoric strain as compression continues, despite the uniaxial nature of the DAC. The data quality is continuously improved by this heat treatment up to the final pressure measured in this experiment of 88 GPa [29] and shows no evidence of chemical reaction or decomposition (Fig. 1).

In addition, we perform quantum simulations of both ice-VII and ice-X using Kohn-Sham DFT. Calculations were performed with the VASP code [32], using the Perdew-Burke-Ernzerhof (PBE) generalized gradient approximation functional [33], and projector-augmented wave pseudopotentials [34,35]. We note that the PBE functional employed here is shown to yield good agreement with experimental results for ice properties at high pressure [36], particularly under the intense conditions of giant planetary interiors [37]. We also found that functionals that include van der Waals interactions yield similar transition pressures from ice-VII to ice-X with the PBE functional [29]. In this paper, the relative Raman intensities for individual ice structures are determined from the derivative of the macroscopic dielectric tensor, computed from the finite-difference method with forward and backward displacements along each vibrational eigenmode [38]. Please see the Supplemental Material for additional details [29].

III. RESULTS

The onset of ice-VII is thus determined by heat treating immediately upon its coexistence with ice-VI (Supplemental Material [29]). Control of pressure from the membrane-driven DAC allows incremental compression until the onset of phase coexistence is evident from XRD. The resulting sample comprises ice-VII only, giving an accurate determination of the

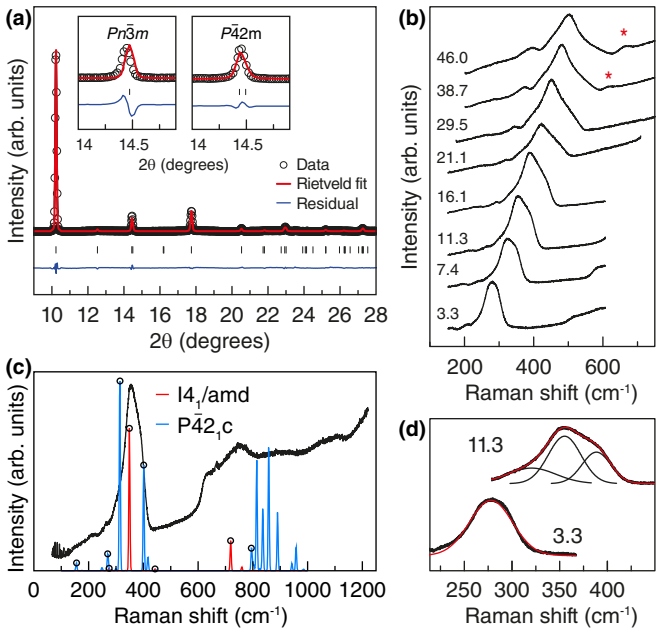

FIG. 2. Evidence for ice-VII$_t$. (a) Rietveld refinement of ice-VII$_t$ $P\bar{4}2m$ at 6.5 ± 0.5 GPa Inset, left: Rietveld refinement of the (2 0 0) Bragg peak using a cubic cell ($Pn\bar{3}m$); right: improvement when using a tetragonal cell ($P\bar{4}2m$). (b) Progression of Raman features on increasing pressure. The dominant mode near 280 cm^{-1} exhibits asymmetry above 5 GPa, and tends back to a single mode above 21 GPa. Red asterisks (*) denote the emergence of the ice-X T_{2g} Raman mode. (c) Simulated Raman spectra at 0 K for two DFT computed ice-VII$_t$ structures compared to the experimental spectra, both at approximately 10 GPa. (d) Dominant Raman feature of ice-VII at 3.3 GPa fit to a single peak whereas the feature in ice-VII$_t$ at 11.3 GPa requires a triplet to fit in agreement with the simulated spectra.

starting volume, V_P, at the lower bound of its thermodynamic stability field. Only from 2.7 ± 0.4 GPa, can we unambiguously index and refine a single phase as cubic ice-VII. Above 5.1 ± 0.5 GPa, we observe deviations in the peak positions and profiles when fitting the XRD patterns to a cubic ice-VII model both before and – more clearly – after heat treating. This is most prominently shown by the Bragg feature at approximately 14.5°, which displays splitting between the (2 0 0)/(0 0 2) which are not accommodated by the cubic ice-VII ($Pn\bar{3}m$) structure. Figure 2(a) shows the Bragg feature at ∼14.5°, where these deviations are most pronounced. Furthermore, a Bayesian analysis is applied to the unit cell data by examining the peak positions and profiles of all ∼7 diffraction features observed and comparing the probability of a cubic structure against a tetragonal structure. The results of which strongly favor a tetragonal model above 5 GPa, which we name here ice-VII$_t$ [29]. We find that this transition from ice-VII to ice-VII$_t$ is accompanied by a $2.18 \pm 0.01\%$ volume discontinuity of the unit cell at 5 GPa [29]. The discrepancy in transition pressures between our tetragonal model and the previously named disordered ice VII′ emphasize the influence of nonisotropic stress components in high-pressure experiments on ice as well as isotope effects [11,14,16,24,25].

We further investigate our observation of ice-VII$_t$ by preparing new samples for Raman spectroscopy experiments, the results of which are consistent with the tetragonal structure above 5 GPa. We first observe the lattice modes of ice-VII near 3.3 GPa after heat treatment of the solidified sample [Fig. 2(b)]. This spectrum is dominated by a feature at 280 cm^{-1} fit to a single mode and also includes a weaker mode at 211 cm^{-1} [Fig. 2(b)]. Due to the close similarities between the Raman spectra of proton-disordered ice-VII and proton-ordered ice-VIII, these modes were previously assigned to the analogous translational-vibration modes of ice-VIII, B_{1g} and A_{1g}, respectively [17,39]. We also observe a very weak mode which has not been previously reported near 160 cm^{-1} [29]. Features were also observed in the 500 cm^{-1} to 800 cm^{-1} range, corresponding to the known E_g and B_{2g} modes [17,29].

Beginning around 5.0 GPa, the dominant feature near 280 cm^{-1} displays an increasingly asymmetric profile [Figs. 2(b)–2(d)]. The appearance of new lattice modes [Fig. 2(c)] is consistent with a lowering of symmetry from the cubic $Pn\bar{3}m$ space group to the tetragonal space group. We confirm this with our DFT calculations in Fig. 2(c), where the combined simulated Raman spectra of two ice-VII configurations with body-centered tetragonal symmetry are needed to explain the broad feature centered at ∼280 cm^{-1} as well as the manifold of peaks above 700 cm^{-1} in the measurements. This supercell solution is required due to the partial occupancy of the hydrogen and oxygen sites, which is imperative in describing this phase of ice. The asymmetry of the observed experimental profile at 280 cm^{-1} is sustained until approximately 21.1 GPa, after which the peak profile becomes increasingly symmetric [Fig. 2(b)].

We then map our DFT-determined tetragonal supercells onto their single (two molecule) primitive unit cell to compare the DFT structure to our XRD data [29]. This results in a space group of $P\bar{4}2m$ body-centered tetragonal structure that is equivalent to a slightly distorted ice-VII structure with noncubic oxygen sites. Applying this tetragonal solution significantly improves the Rietveld refinement of our XRD data ($wR_P = 1.78\%$ and $R_P = 1.38\%$) to model our XRD data, resulting in cell parameters $a = 3.2231 \pm 0.0002$ Å and $c = 3.2357 \pm 0.0003$ Å [Fig. 2(a) inset], further supporting the presence of ice-VII$_t$.

By 38.7 GPa, a new feature is clearly observed in the Raman spectra of ice at 618 cm^{-1} [Figs. 2(b) and 3(a)-(c)], the intensity of which increases with pressure and disappears upon decompression with little hysteresis [Fig. 3(b)]. We interpret this new mode as the T_{2g} mode, which signifies the onset of H-bond symmetrization in ice-X [12,40]. The clear reversibility of the appearance/disappearance of this mode signals that this is a purely pressure-driven phenomenon which is expected for the ice-X transition [Fig. 3(b)]. Furthermore, there is a noticeable stiffening of the frequency of the lattice modes, shown in Fig. 3(a), following the emergence of this new peak, in agreement with the significant mode strengthening which occurs at the onset of ice-X. The blueshifting and broadening of librational and lattice modes due to symmetrization of the hydrogen bond is seen in a number of hydrides [41], including water [10].

Similar observations of the emergence of the T_{2g} mode previously confirmed the transition from ice-VIII to ice-X [40] at liquid nitrogen temperatures, albeit at a slightly shifted frequency from our measurements, as expected from the tem-

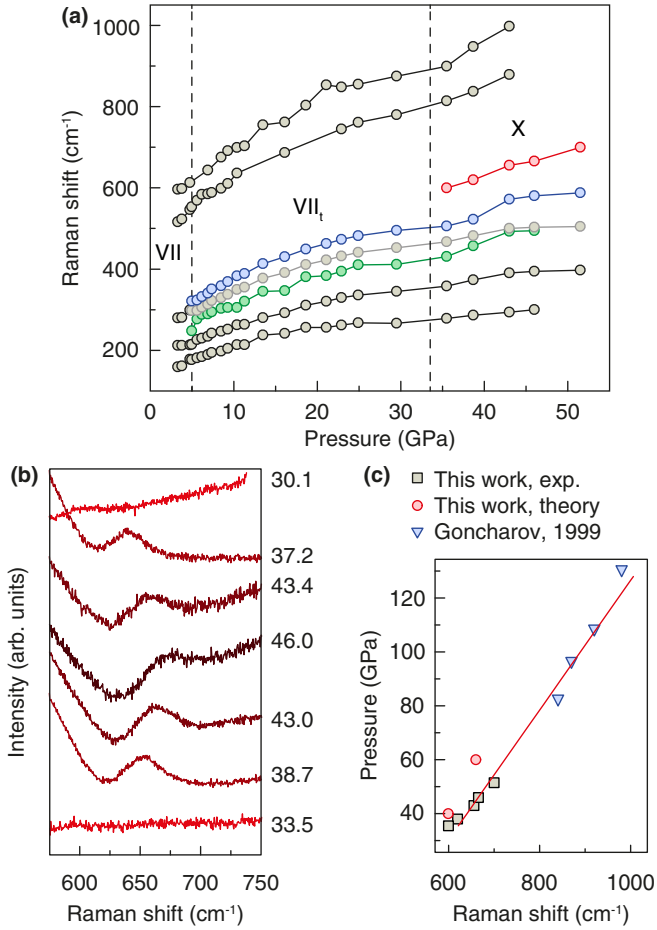

FIG. 3. Raman spectrum of heat-treated H_2O ices under compression. (a) Frequency shift of measured Raman modes of H_2O ice with pressure. Splitting of the dominant lattice mode near 280 cm^{-1} due to tetragonal distortion above 5 GPa is highlighted in blue and green. Red points show the emergence of the ice-X T_{2g} mode above 33 GPa. Dashed lines represent transition pressures based on analysis of XRD data. (b) Bottom to top: Development of ice-X T_{2g} mode on compression above 33 GPa and its reversible disappearance on decompression. (c) Frequency shift of ice-X T_{2g} Raman mode with pressure as determined by this study (experimentally and theoretically) and an interpolating line, as a guide, connecting to those reported by Goncharov *et al.* [12] at higher pressures.

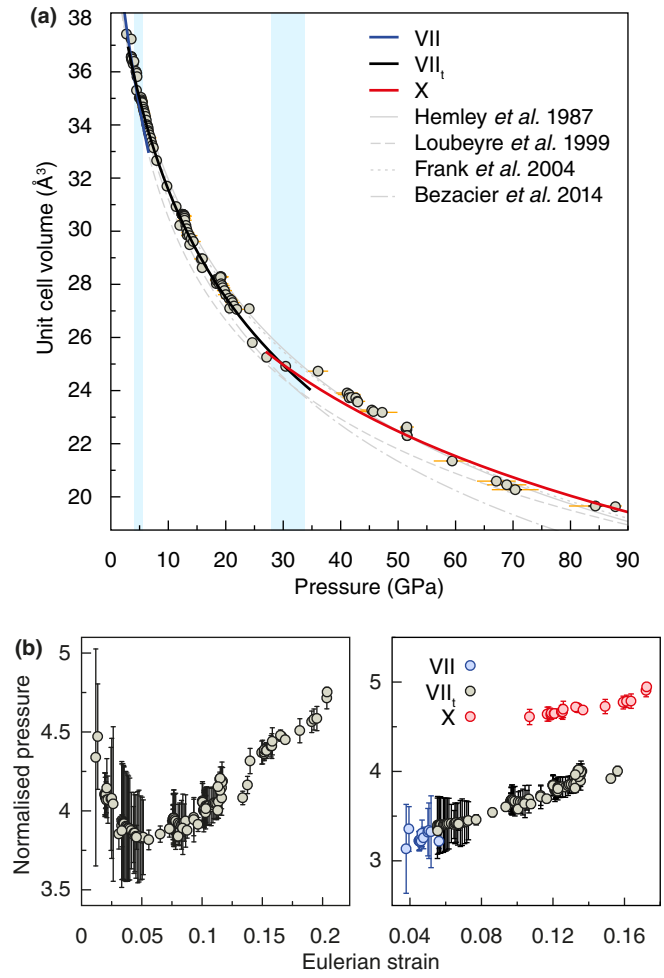

FIG. 4. Equation of state fitting. (a) Pressure-volume plot of our data and Vinet EOS fit from MCMC for the three phases. The calculated uncertainties in transition pressures are indicated by the blue shaded regions at 5.1 ± 0.5 GPa and 30.9 ± 3 GPa, respectively, and the grey lines are results from previous experiments. Curves are color coded by phase (blue: cubic ice-VII; black: noncubic ice-VII$_t$; and red: ice-X. Orange error bars indicate our systematic uncertainty from deviatoric stresses in non-heat-treated data. (b) Linearized Vinet EOS. Left: When assuming a single phase model. Right: When assuming a three-phase model.

perature and density differences. Due to the aforementioned similarities between the Raman spectra of ice-VII and ice-VIII [17,39], this agreement supports our claim of a transition to the symmetric H bonds at similar pressures.

We confirm our interpretation of the T_2g mode with DFT simulations of the ice-X Raman spectrum. The simulations show the appearance of a peak at close to 618 cm^{-1} that is absent from all other simulated ice spectra in this paper, including cubic ice-VII and ice-VIII. The frequency of this mode is tracked with pressure to 51.5 GPa and is in agreement with our computed Raman spectra and earlier measurements on ice-X made by Goncharov *et al.* [12] above 80 GPa as shown in Fig. 3(c).

The consistency in findings between the three independent tools used in this study (XRD, Raman spectroscopy, and DFT calculations) gives us confidence in our findings of a crystal structure of tetragonal symmetry near 5 GPa and the onset of ice-X above 30 GPa. With this insight, we fit a three-phase *P-V* Vinet EOS to the data using Markov chain Monte Carlo (MCMC). This model optimizes the EOS fit parameters based on the values obtained from least-squares fitting [29] and also includes two transition pressures as fitting parameters. The results of our three phase EOS fit are as follows: ice-VII ($K_0 = 18.47 \pm 4.00$ GPa), ice-VIIt ($K_0 = 20.76 \pm 2.46$ GPa) and ice-X ($K_0 = 50.52 \pm 4.16$ GPa) are shown with the calculated transition pressures in Fig. 4(a). Our calculated transition pressure of ice-X at 30.9 ± 3 GPa [Fig. 4(a)] corresponds well with the emergence of the T_{2g} mode in our Raman experiment as well as the discontinuity in bulk modulus shown in Méndez *et al.* [22]. Importantly, fitting of the region above 30.9 ± 3 GPa displays a 2.5X lowering in compressibility, signifying a major change in the bonding character of ice.

In contrast, our DFT calculations (0 K structural optimization, with ions treated as classical particles) show a pressure transition from ice-VII to ice-X at ∼90 GPa, in agreement with previous calculation studies [42–44]. However, it has been reported that the inclusion of the quantum nuclear vibrational effects on the nuclei can lower the transition pressure from the classical limit of 100 GPa to 30 GPa due to the proton being delocalized between the two sites on either side of the bond [23,45,46]. This is consistent with our estimated experimental observation of the onset of ice-X at 30.9 GPa.

The validity of this three-phase model is best highlighted with the linearized form of the Vinet EOS relating the normalized pressure to Eulerian strain [47], which is sensitive to the starting phase volume, V_0. Using V_0 from a single-phase fit to ice-VII fails to describe the compressibility across the entire pressure range as seen by the abnormal curvature in Fig. 4(b) (left). Conversely, linear trends appear when modeling with three distinct phases and their fitted EOS parameters [Fig. 4(b) (right)], signifying that the fit properly describes the P-V data.

IV. DISCUSSION AND CONCLUSION

The results of our multiphase fit show that room temperature H_2O takes the form of cubic ice-VII as a single phase from 2.7 ± 0.4 to 5.1 ± 0.5 GPa, followed by tetragonal ice-VII_t to 30.9 ± 3 GPa, and the likely onset of H-bond symmetrization thereafter. These calculated phase boundaries are reinforced by independent observations in our Raman spectroscopy study and DFT simulations. The low transition pressure into noncubic ice-VII_t based on an observed lowering of symmetry and simulations, implies that cubic ice-VII is stable for only a small window of phase space—contrary to existing assumptions [48]. Thus the ice-VII_t phase of ice could exist in abundance in the crust and upper mantle of expected water-rich super-earths.

Our results show a more than doubling of the bulk modulus of ice above 30 GPa, which is validated by our analysis of the EOS fitting parameters in Fig. 4(b). This discontinuous change in bulk modulus with respect to pressure implies a phase transition of at least third order or lower [49]. A strong (2.5X) increase in bulk modulus signifies a dramatic increase in bond strength of the system [50]. This increased bond strength is unlikely to be accommodated by the H-bonded network of ice-VII or ice-VII_t. This may be indicative of the onset of a stronger bonding taking place like a mix of covalent and ionic bonding which occurs in the H-bond symmetrization of the H_2O system.

The scattering power of hydrogen is too weak from XRD techniques to provide sufficient quantifiable information on the hydrogen's atomic position. Neutron crystallography is capable of accurately measuring the atomic positions in high pressure ice. However, these are limited to only studying deuterated samples, D_2O, as protons have a large incoherent scattering and negative scattering length. While measurements of D_2O are important, isotope effects in water are well-known to shift transition lines. For example, the shift in the transition line of ice-VI to VII [51] at low pressures, and it is likely to have an even stronger effect on the H-bond symmetrization pressure due to the doubled mass of the deuteron and quantum behavior of ice leading up to the transition.

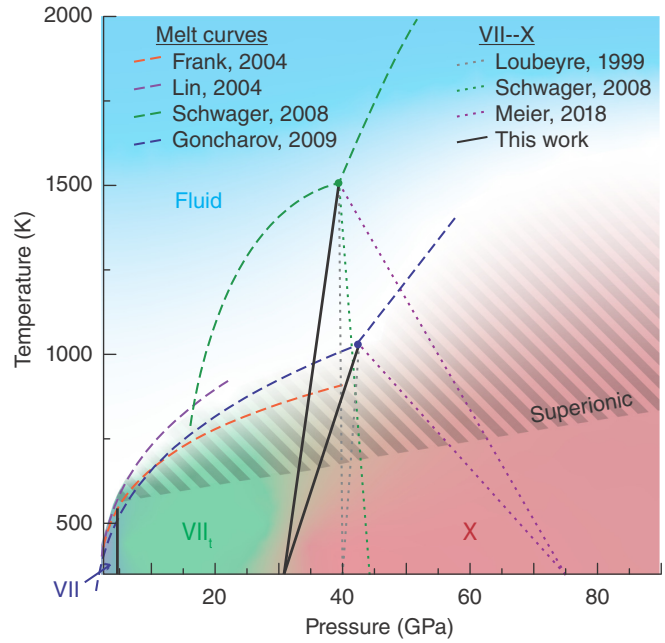

FIG. 5. Phase diagram of ice. Dark blue-, green-, and red-shaded regions denote ice-VII, VII_t and X, respectively, and projected phase boundaries separating high-pressure ice phases from our work are shown as solid black lines. Ice-X phase boundaries connect our measured transition at 30.9 ± 3 GPa and 300 K to the inflection point in the melt curve observed by Schwager and Boehler [53] and Goncharov *et al.* [54], which have been associated with the transition from molecular to ionic fluid. The same procedure has been used to project phase boundaries from Loubeyre *et al.* [13] and Meier *et al.* [18] In doing so, we deduce a steep, positive Clapeyron slope defining the transition from hydrogen bonding to ionic bonding in dense H_2O, consistent with a pressure-driven change in bonding nature. Dashed lines show measured melting curves [53–56]. Superionic boundary from Sugimura *et al.* [57] is highlighted.

Our Raman spectroscopy data shows a clear, reversible transition at the same pressures as the XRD data. This implies a lower (first or second) order phase transition has taken place. We interpret this mode as the T_{2g} mode, the only Raman active mode of ice-X. We confirm this by calculating the frequency for the T_{2g} mode at pressure and show they are in agreement with the measured frequency in Fig. 3(c). Furthermore, drawing an interpolating line between our measured pressure shift of the frequency with that of Goncharov *et al.* [12] shows a similar trend as seen in Fig. 3(c). However, we must acknowledge that the appearance of the T_{2g} mode does not coincide with the disappearance of the ice-VII_t modes. This is an unexpected result given that ice-X only has the single active Raman mode. This result is also found in previous measurements by Goncharov *et al.* [12], where the T_{2g} mode is shown with comparable intensity as the ice-VII_t Raman modes past 80 GPa and only after approximately 94 GPa does the single ice-X mode dominate the presented spectra. This can be interpreted as possible phase coexistance but our XRD data does not support such a claim. Rather this is likely a sign of an intermediate state resulting from an effective centering of the proton due to tunneling effects before the collapse to a single well potential in fully ordered ice-X.

The studies on H_2O by Meier *et al.* [18] and Trybel *et al.* [23] show that beginning as low as 20 GPa, the protons exhibit a significant tunneling effect between the double well of the H bond. This tunneling probability is shown to increase with pressure as the O—O distance decreases, causing an effective centering in what they label ice X′. Our heat-treatment technique improves our sample quality allowing us to observe this subtle transition by means of XRD and Raman scattering. These differ from the findings in neutron studies but we suspect these differences mostly arise due to the doubled mass of the deuteron, which significantly dampens tunneling effects, causing D_2O to behave more classically and pushing the H-bond symmetrization transition to a higher pressure than in H_2O. However, the disparity between our results and those of previous studies on H_2O is likely due to our alleviation of strain in the sample which may be an inhibitor to the transition to symmetric H bonds. There is also the possibility that the other studies had contamination from an ionic species in their water samples which is shown to push the transition pressure of ice-X to higher pressures [52].

We conclude that H_2O in the mixed ionic/covalent bond regime (ice-X or X′) is 2.5X less compressible ($K_0 = 50.52 \pm 4.16$ GPa) than in the H-bond regime of ice-VII ($K_0 = 18.47 \pm 4.00$ GPa) and the presently reported ice VII$_t$ ($K_0 = 20.76 \pm 2.46$ GPa). These results require a significant redrawing of the high-pressure phase diagram of ice, as we show in Fig. 5. The increased proton mobility which leads to the lower transition pressure to ice-X and ice-VII$_t$ prior likely aids in the lower pressure transition to superionic ice phases at increased temperature [57]. There is also a well-documented inflection in the melt line near 40 GPa [53,54] shown in Fig. 5, which has been associated with a density-driven transition either above the melt line or below. In the case of below the melt line, this would be associated with the transition to ice-X, and we show this phase boundary in Fig. 5. As our recorded transition pressure for ice-X is at much lower pressures than previous measurements, the resulting Clapeyron slope for this transition is a steep positive slope, contrary to prior beliefs.

The reversibility of the change in bonding states on the transition to ice-X makes a strong case for this to be a purely pressure-driven transition. We expect this to diminish the thermodynamic driving force for the geochemical release of water in the earth's crust and upper mantle at similar pressures, effectively trapping water in these physical regions. Although the pressure dependence of H-bond symmetrization in H_2O at high temperature remains to be studied, our discoveries provide a significant benchmark for continued advancements in understanding water at extreme conditions and its role in planetary interior processes.

The dataset from this experimental work can be accessed at [74].

ACKNOWLEDGMENTS

This research was sponsored in part by the National Nuclear Security Administration under the Stewardship Science Academic Alliances program through DOE Cooperative Agreement No. DE-NA0001982. This work was performed at HPCAT (Sector 16), Advanced Photon Source (APS), Argonne National Laboratory. This work was performed under the auspices of the U.S. Department of Energy by Lawrence Livermore National Laboratory under Contract DE-AC52-07NA27344, funded under LDRD number 16-ERD-037. J.S.S. acknowledges the support of DOE-BES/DMSE under Award No. DE-FG02-99ER45775. HPCAT operation is supported by DOE-NNSA under Award No. DE-NA0001974, with partial instrumentation funding by NSF. O.T. acknowledges support from the National Science Foundation under Award No. NSF-EAR 1838330. J.H.S. and J.H.B acknowledge support from NASA Grants No. NNX16AK32G and No. NNX16AK08G. This research made use of the Cherry Creek computer cluster administered by the UNLV National Supercomputing Institute.

[1] A. Dunaeva, D. Antsyshkin, and O. Kuskov, Sol. Syst. Res. **44**, 202 (2010).
[2] M. Millot, F. Coppari, J. R. Rygg, A. C. Barrios, S. Hamel, D. C. Swift, and J. H. Eggert, Nature (London) **569**, 251 (2019).
[3] J. Li and D. Ross, Nature (London) **365**, 327 (1993).
[4] R. M. Hazen, R. T. Downs, and L. W. Finger, Science **272**, 1769 (1996).
[5] K. Hirsch and W. Holzapfel, Phys. Lett. A **101**, 142 (1984).
[6] W. Holzapfel, B. Seiler, and M. Nicol, J. Geophys. Res. Solid Earth **89**, B707 (1984).
[7] F. H. Stillinger and K. S. Schweizer, J. Phys. Chem. **87**, 4281 (1983).
[8] K. Aoki, H. Yamawaki, M. Sakashita, and H. Fujihisa, Phys. Rev. B **54**, 15673 (1996).
[9] A. Goncharov, V. Struzhkin, M. Somayazulu, R. Hemley, and H. Mao, Science **273**, 218 (1996).
[10] A. F. Goncharov, N. Goldman, L. E. Fried, J. C. Crowhurst, I. Feng W. Kuo, C. J. Mundy, and J. M. Zaug, Phys. Rev. Lett. **94**, 125508 (2005).
[11] E. Wolanin, P. Pruzan, J. C. Chervin, B. Canny, M. Gauthier, D. Häusermann, and M. Hanfland, Phys. Rev. B **56**, 5781 (1997).
[12] A. F. Goncharov, V. V. Struzhkin, H.-k. Mao, and R. J. Hemley, Phys. Rev. Lett. **83**, 1998 (1999).
[13] P. Loubeyre, R. LeToullec, E. Wolanin, M. Hanfland, and D. Hausermann, Nature (London) **397**, 503 (1999).
[14] M. Somayazulu, J. Shu, C.-s. Zha, A. F. Goncharov, O. Tschauner, H.-k. Mao, and R. J. Hemley, J. Chem. Phys. **128**, 064510 (2008).
[15] E. Sugimura, T. Iitaka, K. Hirose, K. Kawamura, N. Sata, and Y. Ohishi, Phys. Rev. B **77**, 214103 (2008).
[16] M. Guthrie, R. Boehler, C. A. Tulk, J. J. Molaison, A. M. dos Santos, K. Li, and R. J. Hemley, Proc. Natl. Acad. Sci. USA **110**, 10552 (2013).
[17] C.-S. Zha, J. S. Tse, and W. A. Bassett, J. Chem. Phys. **145**, 124315 (2016).
[18] T. Meier, S. Petitgirard, S. Khandarkhaeva, and L. Dubrovinsky, Nat. Commun. **9**, 2766 (2018).

[19] M. Guthrie, R. Boehler, J. J. Molaison, B. Haberl, A. dos Santos, and C. Tulk, Phys. Rev. B **99**, 184112 (2019).

[20] M. French, M. P. Desjarlais, and R. Redmer, Phys. Rev. E **93**, 022140 (2016).

[21] C. Huang, D. R. Rice, Z. M. Grande, D. Smith, J. S. Smith, J. H. Boisvert, O. Tschauner, A. Salamat, and J. H. Steffen, Mon. Not. R. Astron. Soc. **503**, 2825 (2021).

[22] A. S. J. Méndez, F. Trybel, R. J. Husband, G. Steinle-Neumann, H.-P. Liermann, and H. Marquardt, Phys. Rev. B **103**, 064104 (2021).

[23] F. Trybel, M. Cosacchi, T. Meier, V. M. Axt, and G. Steinle-Neumann, Phys. Rev. B **102**, 184310 (2020).

[24] T. Okada, T. Iitaka, T. Yagi, and K. Aoki, Sci. Rep. **4**, 5778 (2015).

[25] R. J. Nelmes, J. S. Loveday, W. G. Marshall, G. Hamel, J. M. Besson, and S. Klotz, Phys. Rev. Lett. **81**, 2719 (1998).

[26] K. Komatsu, S. Klotz, S. Machida, A. Sano-Furukawa, T. Hattori, and H. Kagi, Proc. Natl. Acad. Sci. **117**, 6356 (2020).

[27] D. Balzar and H. Ledbetter, J. Appl. Crystallogr. **26**, 97 (1993).

[28] R. Hrubiak, S. Sinogeikin, E. Rod, and G. Shen, Rev. Sci. Instrum. **86**, 072202 (2015).

[29] See Supplemental Material at https://link.aps.org/supplemental/10.1103/PhysRevB.105.104109 for further experimental details and information on all calculations performed, which includes Refs. [58–73].

[30] D. Smith, J. S. Smith, C. Childs, E. Rod, R. Hrubiak, G. Shen, and A. Salamat, Rev. Sci. Instrum. **89**, 083901 (2018).

[31] K.-E. Thelning, *Steel and Its Heat Treatment: Bofors Handbook* (Butterworth-Heinemann, Amsterdam, 2013).

[32] G. Kresse and J. Hafner, Phys. Rev. B **47**, 558 (1993).

[33] J. P. Perdew, K. Burke, and M. Ernzerhof, Phys. Rev. Lett. **77**, 3865 (1996).

[34] P. E. Blöchl, Phys. Rev. B **50**, 17953 (1994).

[35] G. Kresse and D. Joubert, Phys. Rev. B **59**, 1758 (1999).

[36] M. Millot, S. Hamel, J. R. Rygg, P. M. Celliers, G. W. Collins, F. Coppari, D. E. Fratanduono, R. Jeanloz, D. C. Swift, and J. H. Eggert, Nat. Phys. **14**, 297 (2018).

[37] M. French, T. R. Mattsson, N. Nettelmann, and R. Redmer, Phys. Rev. B **79**, 054107 (2009).

[38] A. Fonari and S. Stauffer, vasp_raman.py, https://github.com/raman-sc/VASP (2013).

[39] P. Pruzan, J. Chervin, and M. Gauthier, Europhys. Lett. **13**, 81 (1990).

[40] K. Hirsch and W. Holzapfel, J. Chem. Phys. **84**, 2771 (1986).

[41] N. Goldman and L. E. Fried, J. Chem. Phys. **125**, 044501 (2006).

[42] M. Bernasconi, P. L. Silvestrelli, and M. Parrinello, Phys. Rev. Lett. **81**, 1235 (1998).

[43] L. Tian, A. I. Kolesnikov, and J. Li, J. Chem. Phys. **137**, 204507 (2012).

[44] X. Z. Lu, Y. Zhang, P. Zhao, and S. J. Fang, J. Phys. Chem. B **115**, 71 (2011).

[45] M. Benoit, D. Marx, and M. Parrinello, Nature (London) **392**, 258 (1998).

[46] Y. Bronstein, P. Depondt, F. Finocchi, and A. M. Saitta, Phys. Rev. B **89**, 214101 (2014).

[47] R. J. Angel, Rev. Mineral. Geochem. **41**, 35 (2000).

[48] W. Holzapfel, J. Chem. Phys. **56**, 712 (1972).

[49] G. Jaeger, Archive History Exact Sci. **53**, 51 (1998).

[50] M. Born and K. Huang, *Dynamical Theory of Crystal Lattices* (Clarendon Press, North Carolina, 1954).

[51] C. W. Pistorius, E. Rapoport, and J. Clark, J. Chem. Phys. **48**, 5509 (1968).

[52] L. E. Bove, R. Gaal, Z. Raza, A.-A. Ludl, S. Klotz, A. M. Saitta, A. F. Goncharov, and P. Gillet, Proc. Natl. Acad. Sci. **112**, 8216 (2015).

[53] B. Schwager and R. Boehler, High Press. Res. **28**, 431 (2008).

[54] A. F. Goncharov, C. Sanloup, N. Goldman, J. C. Crowhurst, S. Bastea, W. Howard, L. E. Fried, N. Guignot, M. Mezouar, and Y. Meng, J. Chem. Phys. **130**, 124514 (2009).

[55] M. R. Frank, Y. Fei, and J. Hu, Geochim. Cosmochim. Acta **68**, 2781 (2004).

[56] J.-F. Lin, B. Militzer, V. V. Struzhkin, E. Gregoryanz, R. J. Hemley, and H.-k. Mao, J. Chem. Phys. **121**, 8423 (2004).

[57] E. Sugimura, T. Komabayashi, K. Ohta, K. Hirose, Y. Ohishi, and L. S. Dubrovinsky, J. Chem. Phys. **137**, 194505 (2012).

[58] R. Hemley, A. Jephcoat, H. Mao, C. Zha, L. Finger, and D. Cox, Nature (London) **330**, 737 (1987).

[59] B. Kamb and B. L. Davis, Proc. Natl. Acad. Sci. USA **52**, 1433 (1964).

[60] J.-L. Kuo, J. V. Coe, S. J. Singer, Y. B. Band, and L. Ojamäe, J. Chem. Phys. **114**, 2527 (2001).

[61] J.-L. Kuo and S. J. Singer, Phys. Rev. E **67**, 016114 (2003).

[62] J. D. Bernal and R. H. Fowler, J. Chem. Phys. **1**, 515 (1933).

[63] G. Kresse and J. Hafner, Phys. Rev. B **49**, 14251 (1994).

[64] G. Kresse and J. Furthmüller, Comput. Mater. Sci. **6**, 15 (1996).

[65] G. Kresse and J. Furthmüller, Phys. Rev. B **54**, 11169 (1996).

[66] J. P. Perdew, K. Burke, and M. Ernzerhof, Phys. Rev. Lett. **78**, 1396(E) (1997).

[67] H. J. Monkhorst and J. D. Pack, Phys. Rev. B **13**, 5188 (1976).

[68] N. Goldman, E. J. Reed, and L. E. Fried, J. Chem. Phys. **131**, 204103 (2009).

[69] B. Santra, J. Klimeš, A. Tkatchenko, D. Alfè, B. Slater, A. Michaelides, R. Car, and M. Scheffler, J. Chem. Phys. **139**, 154702 (2013).

[70] D. Foreman-Mackey, D. W. Hogg, D. Lang, and J. Goodman, Publ. Astron. Soc. Pac. **125**, 306 (2013).

[71] J. H. Boisvert, B. E. Nelson, and J. H. Steffen, Mon. Not. R. Astron. Soc. **480**, 2846 (2018).

[72] S. M. Dorfman, V. B. Prakapenka, Y. Meng, and T. S. Duffy, J. Geophys. Res. **117**, B08210 (2012).

[73] B. E. Nelson, P. M. Robertson, M. J. Payne, S. M. Pritchard, K. M. Deck, E. B. Ford, J. T. Wright, and H. T. Isaacson, Month. Notice. R. Astron. Soc. **455**, 2484 (2016).

[74] Z. M. Grande and A. Salamat, Dataset for: Pressure-driven symmetry transitions in dense H_2O ice (Zenodo, 2022), https://doi.org/10.5281/zenodo.6339621.